

# Secondary radiation measurements for particle therapy applications: prompt photons produced by $^4\text{He}$ , $^{12}\text{C}$ and $^{16}\text{O}$ ion beams in a PMMA target

I. Mattei<sup>a</sup>, F. Collamati<sup>b</sup>, E. De Lucia<sup>b</sup>, R. Faccini<sup>c,d</sup>,  
 P. M. Frallicciardi<sup>e</sup>, C. Mancini-Terracciano<sup>c,d</sup>, M. Marafini<sup>d,f</sup>,  
 S. Muraro<sup>a</sup>, R. Paramatti<sup>d</sup>, V. Patera<sup>d,f,g</sup>, L. Piersanti<sup>d,g</sup>,  
 D. Pinci<sup>d</sup>, A. Rucinski<sup>d,g</sup>, A. Russomando<sup>c,d,h</sup>, A. Sarti<sup>b,f,g</sup>,  
 A. Sciubba<sup>d,f,g</sup>, E. Solfaroli Camillocci<sup>c,d</sup>, M. Toppi<sup>b</sup>,  
 G. Traini<sup>c,d</sup>, C. Voena<sup>d</sup>, G. Battistoni<sup>a</sup>

<sup>a</sup> INFN - Sezione di Milano, Italy

<sup>b</sup> Laboratori Nazionali di Frascati dell'INFN, Frascati, Italy

<sup>c</sup> Dipartimento di Fisica, Sapienza Università di Roma, Roma, Italy

<sup>d</sup> INFN - Sezione di Roma, Italy

<sup>e</sup> Istituto di ricerche cliniche Ecomedica, Empoli, Italy

<sup>f</sup> Museo Storico della Fisica e Centro Studi e Ricerche “E. Fermi”, Roma, Italy

<sup>g</sup> Dipartimento di Scienze di Base e Applicate per Ingegneria, Sapienza Università di Roma, Roma, Italy

<sup>h</sup> Center for Life Nano Science@Sapienza, Istituto Italiano di Tecnologia, Roma, Italy

## Abstract.

Charged particle beams are used in Particle Therapy (PT) to treat oncological patients due to their selective dose deposition in tissues with respect to photons and electrons used in conventional radiotherapy. Heavy ( $Z>1$ ) PT beams can additionally exploit their high biological effect in killing cancer cells. Nowadays, protons and carbon ions are used in PT clinical routine. Recently, the interest on the potential application of helium and oxygen beams is growing: with respect to protons such beams are characterized by their reduced multiple scattering inside the body and increased linear energy transfer, relative biological effectiveness and oxygen enhancement ratio.

The precision of PT demands for online dose monitoring techniques, crucial to improve the quality assurance of treatments: possible patient mis-positionings and tissues biological changes with respect to the CT scan could negatively affect the therapy outcome. The beam range confined in the irradiated target can be monitored thanks to the neutral or charged secondary radiation emitted by the interactions of hadron beams with matter. Among these secondary products, prompt photons are produced by nuclear de-excitation processes and, at present, different dose monitoring and beam range verification techniques based on the prompt- $\gamma$  detection have been proposed. It is hence of importance to perform the  $\gamma$  yield measurement in therapeutical-like conditions.

In this paper we report the yields of prompt photons produced by the interaction of helium, carbon and oxygen ion beams with a poly-methyl methacrylate (PMMA) beam stopping target. The measurements were performed at the Heidelberg Ion-Beam

Therapy center (HIT) with beams of different energies. A LYSO scintillator, placed at  $60^\circ$  and  $90^\circ$  with respect to the beam direction, has been used as photon detector. The obtained  $\gamma$  yields for carbon ion beams are compared with results from literature, while no other results from helium and oxygen beams have been published yet. A discussion on the expected resolution of a slit camera detector is presented, demonstrating the feasibility of a prompt- $\gamma$  based monitoring technique for PT treatments using helium, carbon and oxygen ion beams.

## Introduction

Particle Therapy (PT) exploits the characteristic energy release in matter of charged particles, mainly protons and carbon ions, in the irradiation of tumor volumes trying to spare as much as possible the surrounding healthy tissues. In comparison to the most advanced photon radiotherapy technique, protons and carbon ions have the advantageous feature of a high Linear Energy Transfer (LET) and increased Relative Biological Effectiveness (RBE), which make those particles particularly favourable in treating radio-resistant tumors (Loeffler & Durante 2013). Beside protons and carbon ions, helium and oxygen ion beams are currently investigated as PT candidates (Tommasino et al. 2015): helium ions suffer less lateral multiple scattering with a consequent reduced beam broadening with respect to protons, providing a good solution in the irradiation of radio-resistant tumors when low beam fragmentation is required (Fuchs et al. 2014). Oxygen ions could be of advantage when increasing efficiency in treating radio-resistant tumors is needed due to their higher LET, RBE and Oxygen Enhancement Ratio (OER) with respect to protons, carbons and heliums (Kurz et al. 2012).

The high selectivity of PT makes this technique particularly sensitive to possible patient mis-positionings and anatomical variations, asking for the development of an online beam range monitor. This should be able to provide a feedback on the dose deposition spatial distribution during the treatment in order to improve its quality and efficacy: the lack of a precise online monitoring is one of the key issues to be addressed to support the diffusion of PT therapies in clinical centers. The beam range monitoring takes advantage of the secondary radiation produced by the interactions of the beam with the target nuclei along the path inside the target volume: the beam is stopped inside the patient and the secondaries escaping from the body can be detected, their emission profile reconstructed and used to monitor the beam dose deposition and range. So far, the most established PT beam monitoring technique is based on the detection of back-to-back photons produced by the annihilation positrons coming from  $\beta^+$  emitters (PET photons) using the Positron Emission Tomography (PET) technique. Nevertheless, the signal level is lower in comparison with PET signals known from clinical diagnostics, and at present such technique is used off-line, after the patient irradiation, aiming for further investigation methods (Parodi et al. 2008).

A technology capable of on-line PET detection (Pawelke et al. 1997, Parodi et al. 2002, Priegnitz & *et al.* 2008, Fiedler et al. 2008) is currently under development (Attanasi et al. 2009, Vecchio et al. 2009, Marafini & *et al.* 2015, Pennazio & *et al.* 2015). The characterization of the secondary radiation produced by p and  $^{12}\text{C}$  beams of therapeutic energy has been the subject of an intensive experimental campaign in the recent past: the production of PET photons (Enghardt et al. 2004, Agodi et al. 2012*c*), light charged fragments (Agodi et al. 2012*a*, Henriquet et al. 2012, Gwosch et al. 2013, Piersanti et al. 2014) and prompt photons, main object of this contribution, has been studied in different experimental conditions (Kraan 2015). In particular, the prompt- $\gamma$  production has been recently investigated by several experiments performed using p and  $^{12}\text{C}$  beams of several energies: 73 MeV/u (Testa et al. 2008, Testa et al. 2009), 80 MeV/u (Agodi et al. 2012*b*, Agodi et al. 2013), 220 MeV/u (Mattei et al. 2015), 95 MeV/u, 300 MeV/u and 310 MeV/u (Pinto et al. 2015, Testa et al. 2010). The prompt- $\gamma$  yield estimation is of particular importance since it strongly affects the achievable resolution on the evaluation of the hadron beam range. The main interests in using this kind of secondary radiation for monitoring purposes are related to its large abundance and the high precision achievable on the emission point reconstruction in absence of multiple scattering interactions.

In this paper we present the results of prompt photons production measurements performed using  $^4\text{He}$ ,  $^{12}\text{C}$  and  $^{16}\text{O}$  beams, available at the Heidelberg Ion-beam Therapy center (HIT, Heidelberg, Germany), interacting with a beam stopping PMMA target.

The experimental setup used for the data acquisition is described in detail in § 1, while the results obtained with the LYSO detector at  $60^\circ$  and  $90^\circ$  with respect to the beam direction are discussed in § 2 and compared with the results available from literature. The discussion of the measured fluxes in the context of monitoring applications can be found in § 3, taking as a reference detector for prompt gamma monitoring the IBA knife edge slit camera. Particular care has been made to quantify the impact of the collectable statistics of prompt photons emitted in Particle Therapy with heavy ions clinical like scenarios on the precision achievable on the dose deposition monitoring.

The experimental apparatus did not allow a measurement of the prompt photons production position and hence a disentangling of the photons production induced by the primary incoming radiation and of the secondary photons produced after the Bragg Peak region was not possible. The implications for the prompt photons monitoring are detailed in § 3.

## 1. Experimental setup

The experiment was performed at the HIT center where different ion species of several energies were used to irradiate a poly-methyl methacrylate (PMMA) target to study the prompt- $\gamma$  radiation emitted from the interactions of the beam projectiles with the

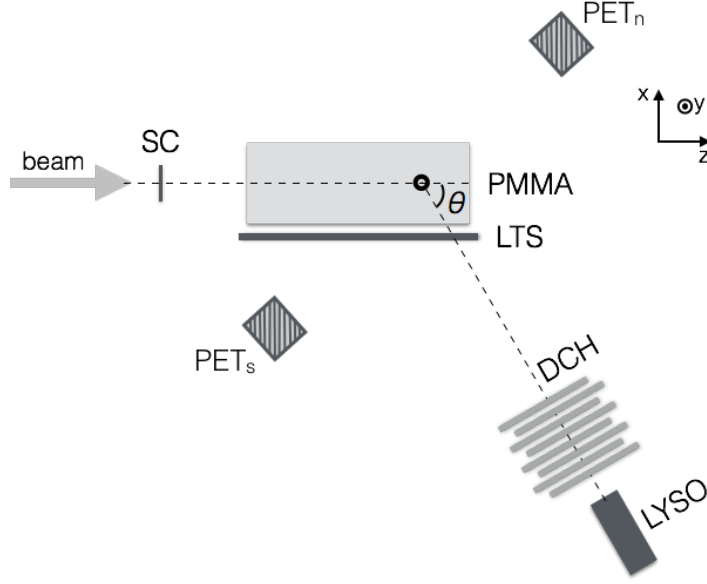


**Figure 1.** Experimental setup scheme (not to scale). The LYSO and DCH detectors were mounted on a movable arm that allowed to detect the secondary radiation in two different angular configurations:  $\theta = 60^\circ$  or  $90^\circ$ , where  $\theta$  is the angle with respect to the beam direction in the horizontal plane.  $\gamma$ -PET detectors ( $PET_s$  and  $PET_n$ ) are also shown.

target nuclei.

Figure 1 shows the experimental setup, which is part of a more extended geometry meant to measure not only the prompt photon radiation, but also secondary charged particles, PET photons and forward emitted heavy fragments.

The origin of the reference frame is marked by the black spot inside the PMMA target. The beam, coming from the left along the  $z$  axis, is illustrated with an arrow. To detect the incoming primary particles, a plastic scintillator (EJ200) 2 mm thick (Start Counter, SC) was placed  $\sim 30$  cm upstream the PMMA. The SC was read by two photomultiplier tubes (PMTs) - Hamamatsu H6524 - each one giving a recorded signal (SC1, SC2). The SC, used as a trigger detector, provided the number of impinging ions and the reference time for the Time of Flight (ToF) measurements.

The PMMA target dimensions are  $(5.00 \times 5.00 \times t_{\text{PMMA}})$   $\text{cm}^3$ , where  $t_{\text{PMMA}}$  is the PMMA thickness that depends on the penetration depth of the primary beam and experimental setup configuration used during the data acquisition (see Table 1). The uncertainty on  $t_{\text{PMMA}}$  is 0.01 cm. For the  $^4\text{He}$  and  $^{16}\text{O}$  ions data collection, in order to keep the Bragg Peak (BP) position fixed for all the beam energies, the size of the PMMA was changed according to the energy and range (BP depth) of each beam. For the carbon ion data acquisition the PMMA thickness was fixed at 10.00 cm regardless of the incoming beam energy, still ensuring that the beam stops within the PMMA.

A Long Thin Scintillator (LTS)  $(0.2 \times 5.0 \times 17.0)$   $\text{cm}^3$ , read by a H10580 PMT, was placed on the PMMA lateral face in order to identify and study secondary charged

particles. A 21 cm long Drift CHamber (DCH) was mechanically aligned with the reference frame origin and was placed at a distance of  $\sim 60$  cm from the PMMA center. The DCH, described in details in (Abou-Haidar et al. 2012, Agodi et al. 2012a, Piersanti et al. 2014), was used to identify and reject the background from low energy charged particles (see § 2).

Prompt photons were detected by a  $2 \times 2$  matrix of scintillating lutetium yttrium orthosilicate (LYSO) crystals,  $(1.5 \times 1.5 \times 12.0)$  cm<sup>3</sup> each, described in detail in (Agodi et al. 2012b). The detector was placed  $\sim 2$  cm behind the DCH exit face and was mechanically aligned with the reference frame origin. In order to discriminate the LYSO signal from the LYSO intrinsic background, a PMT threshold has been set corresponding to a calibrated LYSO deposited energy of  $\sim 1$  MeV.

The energy calibration of the LYSO scintillator was performed with the final data acquisition setup at the HIT center using a radioactive source of  $^{60}\text{Co}$ . The data collected have been used to provide the reference point needed for the implementation of a former calibration of the very same crystal that was performed in the range of interest for prompt photons emission studies, with a different experimental setup, and is documented in detail in a separate manuscript (Bellini et al. 2014). A linear calibration curve, up to  $\sim 10$  MeV, is assumed following the results obtained in the extended calibration energy range study presented in (Bellini et al. 2014). The ToF slewing effect induced by the front-end electronics fixed voltage threshold was taken into account following the procedure described in (Agodi et al. 2012b, Agodi et al. 2013).

The DCH and LYSO detectors were attached to the same movable aluminum arm. This arm could be placed at different angles with respect to the beam direction ( $\theta$ ), *i.e.*  $60^\circ$  and  $90^\circ$ , in order to measure the angular dependence of the prompt- $\gamma$  emission. The total distance of the LYSO from the PMMA center was  $(82.0 \pm 0.1)$  cm in the  $90^\circ$  setup and  $(86.5 \pm 0.1)$  cm in the  $60^\circ$  setup.

Fig. 1 shows also the positioning of two LYSO pixellated  $\gamma$ -PET detectors ( $\text{PET}_s$  and  $\text{PET}_n$ ) used to monitor the production of  $\beta^+$  emitters $^\ddagger$  during the PMMA irradiation. The PET trigger line required the coincidence in time of the signals of the LYSO detectors and was independent from the SC signals in order to allow the measurements of the  $\beta^+$  induced activity also when the beam was not impinging on the target.

The  $\gamma$ -PET detectors were included in the simulation of the experimental apparatus and used to provide an independent check on the number of incoming ions, as described in § 2.3.

Table 1 summarizes the measured setup configurations relative to the collected data sample. For each ion species, the beam energy (*Energy*) and spot size ( $B_{FWHM}$ ) as the Full Width at Half Maximum (FWHM) from the HIT libraries are reported (later in the text, the beam energies will be approximated values). The relative error on the HIT beam energies is of  $1.5 \cdot 10^{-3}$  (Parodi et al. 2012). The beam range in PMMA, defined as

$^\ddagger$  The obtained results, as well as the experimental methods, will be the subject of a dedicated manuscript, currently in preparation, and will be hence documented in detail elsewhere.

Ion	Energy (MeV/u)	B <sub>FWHM</sub> (mm)	Range (cm)	t <sub>PMMA</sub> (cm)	$\theta$
<sup>12</sup> C	120.45	7.9	2.88	10.00	90°
	159.99	6.2	4.83		
	180.89	5.5	6.03		
	219.79	4.7	8.33		
<sup>4</sup> He	102.34	9.3	6.68	7.65	60°
	124.78	7.8	9.68	10.00	90° - 60°
	144.63	6.9	12.63	12.65	
<sup>16</sup> O	209.63	4.6	5.78	7.65	90° - 60°
	259.55	3.9	8.38	10.00	
	300.13	3.6	10.68	12.65	

**Table 1.** The beam energy, beam spot size (FWHM), beam range (BP depth) and PMMA thickness used during the data acquisition are listed as a function of the beam ion species and angular configuration ( $\theta$  = angle at which the DCH and LYSO detector were placed with respect to the beam direction).

the BP position depth inside the target (*Range*), was computed using a FLUKA Monte Carlo (MC) simulation (Ferrari et al. 2005, Boehlen et al. 2014, Battistoni et al. 2015). The error on the reported *Range* values is 0.05 cm, determined from the simulated Bragg curves of each beam impinging on a PMMA target (density: 1.19 g cm<sup>-3</sup>; ionisation potential: 74 eV). For each data taking, the PMMA thickness ( $t_{PMMA}$ ) and the DCH - LYSO angular configuration ( $\theta$ ) are also listed.

The Data AcQuisition (DAQ) trigger was provided by the time coincidence of the logic OR of the SC signals (SC1 or SC2) with the LYSO signal. This choice was driven by the need to optimize the data sample collection efficiency and to allow for a measurement of the SC detector efficiency. It has to be noted that the data analysis performed for the prompt photons study requires the AND of the SC1, SC2 signals in all the steps, to minimize the contribution of random electronic noise to the measurement of the number of incoming ions.

All electronic signals were read-out by a VME system (CAEN V2718 VME-PCI bridge) interfaced with a PC for the DAQ. The time and charge information for the signals of all the detectors were acquired using a 19-bit TDC Multi-hit (CAEN V1190B, time resolution of  $\sim 100$  ps), and a 12-bit QDC (CAEN V792N, resolution of  $\sim 0.1$  pC). The digitization of the time information was accomplished by means of a discrimination system in which the digital output signals had a 100 ns width. The impact of this choice in the counting of events with multiple ions impinging on the SC is discussed in detail below (§ 1.1).

The number of impinging ions was counted by means of a VME scaler (CAEN V560 N), using the logic AND of the SC signals (SC1 and SC2, defined as SCAND).

The VME scaler is capable of sustaining an incoming signal rate up to 100 MHz.

### 1.1. Beam description

The ion beams provided by the HIT facility are accelerated using a synchrotron. The incoming beam rate, kept under the 10 MHz limit set by the SC signal discrimination time used for the ToF measurements, ranged from  $\sim 300$  kHz up to  $\simeq 3$  MHz, depending on the ion beam species. Such rate has been heavily reduced with respect to the therapeutical rates in order to allow the experimental data taking.

The beam time profile (*Beam rate*) is shown for  $^4\text{He}$  (left),  $^{12}\text{C}$  (center) and  $^{16}\text{O}$  (right) data samples in Fig. 2 as a function of the elapsed data taking time (*elapsed time*). The spill structure of the beam is clearly visible.

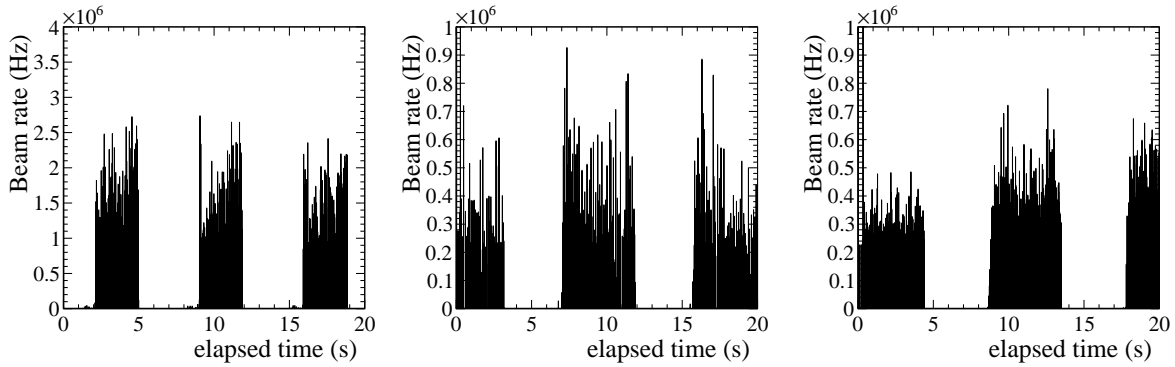


**Figure 2.** The beam time profile for  $^4\text{He}$  (left),  $^{12}\text{C}$  (center) and  $^{16}\text{O}$  (right) data samples as a function of the elapsed data taking time.

The fine structure of the beam, instead, has been measured by means of the multi hit TDC in a  $2\ \mu\text{s}$  window around the trigger time, and it is shown in black dots in Fig. 3 (left) for events collected using the  $^4\text{He}$  beams of 144.63 MeV. Similar spectra have been obtained also for the  $^{12}\text{C}$  and  $^{16}\text{O}$  beams. Using the beam fine structure measured in a time window far from the trigger, e.g. for the  $^4\text{He}$  events in the 200–800 ns window, a MC simulation has been performed in order to account for the inefficiencies, in the detection of multiple ions events, introduced by the fixed time window set by the discriminators used to process the analogic signals from the SC detector. The ions rate used to generate the events in the MC simulation has been tuned to optimize the agreement between the MC (shown as histograms in blue continuous lines) and the data (shown as black dots) measured distributions shown in Fig. 3. A remarkable agreement is observed, allowing a reliable measurement of the discrimination window induced inefficiencies.

The difference in time arrival of multiple ions is shown in Fig. 3 (right), in black dots for the collected data, and shows the inefficiency introduced for ions impinging on the SC with a time distance that is smaller than 100 ns. The red dashed line in Fig. 3 (right) shows the difference in arrival time of all the simulated ions, while the blue

continuous line shows the time difference after the 100 ns discrimination window is taken into account. The systematic uncertainties related to the inefficiencies measurement are discussed in § 2.2.

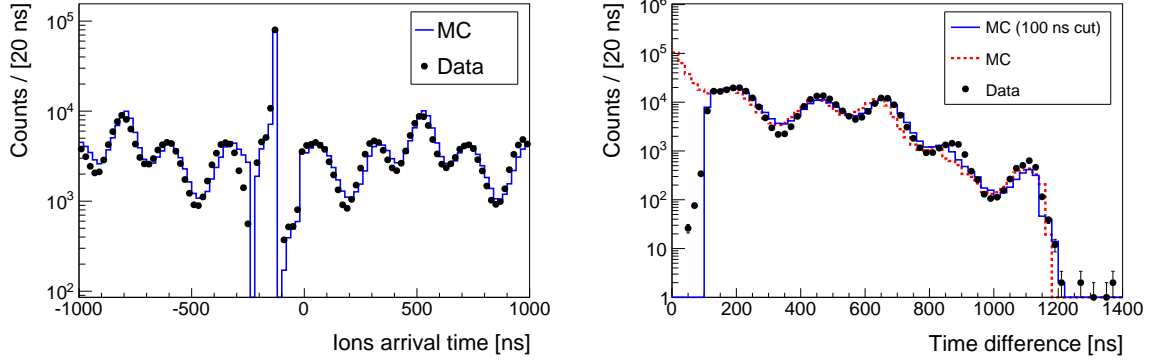


**Figure 3.** Ions arrival time (left) and time difference between the detection of multiple ions (right) are shown for events collected in a time window of 2  $\mu$ s around the trigger time using the  $^4\text{He}$  beam of 144.63 MeV. The data measured distributions are shown in black dots. The output of the dedicated MC simulation used to account for discrimination induced inefficiencies, is superimposed in blue (solid line). The output of a MC simulation that was not including the 100 ns discrimination time window is also shown, in the left figure, in a red dashed line to show the impact on the multiple ions arrival detection.

The beam spot size  $B_{FWHM}$ , as reported in Table 1, is inversely proportional to the beam energy for each ion species. It ranges between 6.9–9.3 mm for  $^4\text{He}$  beams, 4.7–7.9 mm for  $^{12}\text{C}$  beams and 3.6–4.6 mm for  $^{16}\text{O}$  beams.

The maximum trigger rate was 6 kHz, limit set by the DAQ dead time. The trigger lines were set up for the different measurements pointed out at the beginning of § 1: forward fragmentation studies, charged particles and prompt photons production at large angle and  $\beta^+$  emitters production. The trigger line used for the prompt photon studies had a mean rate in the 300 Hz–2 kHz range, depending on the beam conditions, and contributed for the 5%–30% of the total trigger rate.

## 2. Prompt photon yield

The yield of prompt photons produced by the ion beam projectiles interaction with the PMMA target, normalized to the total solid angle and integrated over the full target length, has been computed according to the following equation:

$$\Phi_{\gamma}[\text{sr}^{-1}] = \frac{1}{4\pi} \frac{N_{\gamma}}{N_{\text{ion}} \times \varepsilon_{\text{TOT}} \times \varepsilon_{\text{DT}}} \quad (1)$$

where  $N_{\gamma}$  is the number of prompt photons measured by the LYSO detector in the (2 – 10) MeV energy range,  $N_{\text{ion}}$  is the total number of primary ions impinging



on the PMMA target,  $\varepsilon_{\text{TOT}}$  is the total detector efficiency (including the detector and geometrical contributions) and  $\varepsilon_{\text{DT}}$  is the data acquisition dead time efficiency.

Although the analysis has been performed starting from 1 MeV, the lower limit in the energy range for the yield evaluation was conservatively set to 2 MeV. Above this threshold, the background contribution, mainly due to intrinsic radioactivity of LYSO, electronic noise and neutrons, becomes negligible. The energy upper limit in the yield evaluation was set to 10 MeV: above that energy we expected no significant de-excitation gamma lines from carbon and oxygen nuclei or their residues produced by nuclear reactions (*National Nuclear Data Center - [www.nndc.bnl.gov](http://www.nndc.bnl.gov)*).

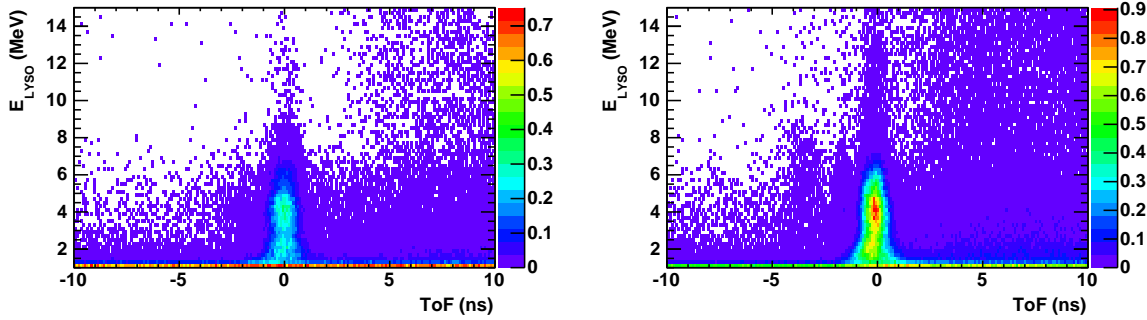


**Figure 4.** Energy deposition in the LYSO crystal as a function of the measured ToF for  $^4\text{He}$  (left) and  $^{16}\text{O}$  (right) events. The data collected at all energies, in the 90 degrees configuration, are summed up and shown for both beam types. The distributions have been normalized to the same number ( $10^7$ ) of incoming beam ions.

The prompt photons number  $N_\gamma$  has been evaluated starting from the 2-dimensional distribution of the deposited energy in the crystal ( $E_{\text{LYSO}}$ ) as a function of the Time of Flight (ToF) of secondaries interacting in the LYSO (see Fig. 4).

The ToF is defined as the time difference between the signal detected in the LYSO and the signal detected in the SC (SCAND) induced by a traversing ion ( $T_{\text{LYSO}} - T_{\text{SCAND}}$ ). In this definition of ToF, the time slewing effect is corrected following the same procedure described in (Agodi et al. 2012b).

Fig. 4 shows, as an example, the  $E_{\text{LYSO}}$  vs ToF distribution used to select the prompt- $\gamma$  signal for the events taken using  $^4\text{He}$  (left) and  $^{16}\text{O}$  (right) ions as projectiles. The distributions have been obtained combining the data obtained in the different energy configurations and collected at 90 degrees. A scaling factor has been applied to both histograms in order to normalize the distributions to the same statistics ( $10^7$  events). The horizontal low energy band visible in both plots ( $E_{\text{LYSO}} < 1.5$  MeV) is related to the LYSO intrinsic noise, while the diffused cloud is associated to neutrons, with a ToF that is almost uncorrelated to the SC signal. The vertical band at 0 ns is relative to the prompt photons signal.

$N_\gamma$  has been computed from the reduced ToF ( $\text{ToF}/\sigma_{\text{ToF}}$ ) distributions, selected in the  $[-10, 10]$  interval and sampled in  $E_{\text{LYSO}}$  bins of  $\sim 0.2$  MeV. The  $\sigma_{\text{ToF}}$  values have been extracted from the time slewing correction procedure, where the ToF distributions

sampled in  $E_{\text{LYSO}}$  bins have been modeled with a gaussian function (more details can be found in (Agodi et al. 2012b)). The number of prompt photons has been extracted from an unbinned maximum likelihood fit, performed using the RooFit toolkit from ROOT (Verkerke & Kirkby 2003), to the reduced time distribution for each energy bin. Fig. 5 shows two examples of reduced time distributions in lower ( $1.4 \text{ MeV} < E_{\text{LYSO}} < 1.6 \text{ MeV}$ , shown in the left) and higher ( $4.6 \text{ MeV} < E_{\text{LYSO}} < 4.8 \text{ MeV}$ , shown in the right) energy bins for a 145 MeV/u helium ion beam run with the LYSO detector placed at  $\theta = 90^\circ$ .

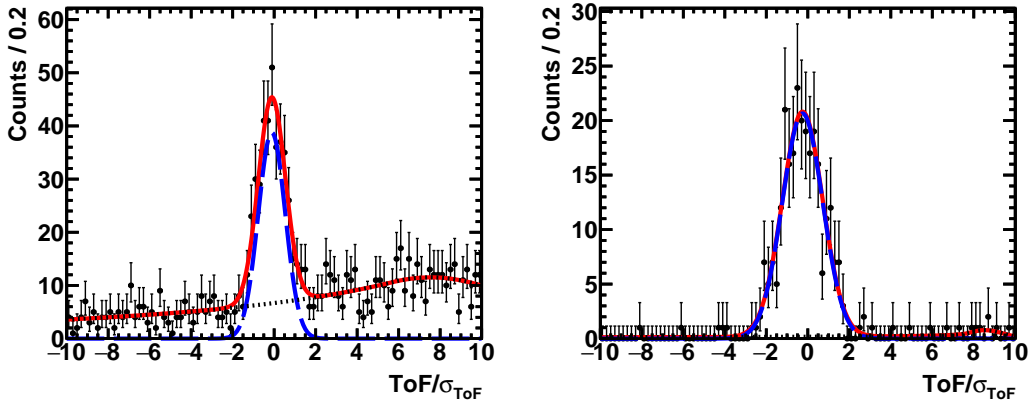


**Figure 5.** Examples of the reduced time distribution in two different energy ranges (left:  $1.4 \text{ MeV} < E_{\text{LYSO}} < 1.6 \text{ MeV}$ ; right:  $4.6 \text{ MeV} < E_{\text{LYSO}} < 4.8 \text{ MeV}$ ) for a 145 MeV/u helium ion beam run in the  $90^\circ$  angular configuration. The dashed line indicates the gaussian fit to the signal while the dotted line is the Crystal Ball function fitting the neutron background.

The total fit function (solid line) is superimposed to the data spectrum: the background, mainly due to neutrons, is described by a Crystal Ball (Skwarnicki 1986) shape (dotted line), while the signal is modeled using a gaussian Probability Density Function (PDF, dashed line). The Crystal Ball function well represents the neutron background, especially in the low energy range ( $E_{\text{LYSO}} \sim 2 \text{ MeV}$ ). The background coming from low energy charged particles has been reduced by requiring that the number of hits detected in the drift chamber ( $N_{\text{hit}}$ ) is less than three (the average number of hits detected for a charged particle traversing the DCH is 12). As a cross-check of the charged particle background relevance in the final result, the LTS detector has been used as an additional veto for charged particles: the combined use of DCH and LTS did not result in a sensible change of the yields and hence we did not explicitly include the LTS charged particles veto in the final analysis.

The dead time (DT) efficiency  $\varepsilon_{\text{DT}}$  has been evaluated using the VME scaler in which all the generated trigger signals ( $N_{\text{TrTot}}$ ) and the triggers signals acquired by the DAQ system ( $N_{\text{TrAcq}}$ ), were counted. The DT efficiency, defined as  $\varepsilon_{\text{DT}} = N_{\text{TrAcq}}/N_{\text{TrTot}}$  varied from 60% to 90%, depending on the beam rate. Average values of  $\varepsilon_{\text{DT}}$  for the different data taking conditions (ion species, beam energies and angular configurations)

have been used to compute the integrated yields using Eq. 1.

The total number of primary ions impinging on the PMMA target is defined as  $N_{\text{ion}} = N_{\text{ion}}^{\text{raw}} \times \text{corr}_{\text{ion}}$  where  $N_{\text{ion}}^{\text{raw}}$  is the number of primary ions computed counting the number of SCAND signals over threshold as described in § 1.

The obtained counts have to be corrected by  $\text{corr}_{\text{ion}}$ , a correction factor that takes into account the inefficiency due to the 100 ns dead time introduced by the width of the SC discriminated signals.

As discussed in § 1.1, and shown in Fig. 3 (right), this correction has been evaluated as the average fraction of lost ions using a dedicated MC simulation tuned in order to reproduce the temporal beam structure of each data set that was acquired.  $\text{corr}_{\text{ion}}$  was measured as the ratio of all the events impinging on the SC, without applying any cut (as shown in Fig. 3 right, red dashed histogram), to the number of events in which the arrival time difference of multiple ions was greater than 100 ns (as shown in Fig. 3 right, blue solid histogram). The measured  $\text{corr}_{\text{ion}}$  values, computed for each data set to take into account the different beam rates, are in the range  $[1.0, 1.5]$ .

### 2.1. MC simulation

The detector and geometrical efficiencies ( $\varepsilon_{\text{TOT}}$ ) have been computed using a MC simulation based on the FLUKA code, that implemented all the experimental configuration (beam characteristics and experimental setup as described in § 1 by Table 1 and shown in Fig. 1).

The total efficiency  $\varepsilon_{\text{TOT}}$  has been defined as the ratio of  $N_{\gamma}^{\text{meas}}$  to  $N_{\gamma}^{\text{gen}}$ , where  $N_{\gamma}^{\text{meas}}$  is the number of prompt photons measured by the LYSO detector, after having applied the same signal selections performed in the experimental data analysis, and  $N_{\gamma}^{\text{gen}}$  is the number of prompt photons produced with energy  $> 2$  MeV by the ion beam interacting with the PMMA target. The computed  $\varepsilon_{\text{TOT}}$  ranges from  $6.6 \cdot 10^{-5}$  up to  $8.6 \cdot 10^{-5}$ , depending on the different experimental setup conditions.

The computed efficiency depends only on the modeling of the prompt photon transport from the production point inside the PMMA target up to the LYSO detector. There is no dependence of the measured efficiency on the nuclear models used in FLUKA to generate the prompt photons emission spectrum as we are only taking into account the attenuation due to the interactions with matter of the emitted photons (related to the positioning and composition of the target and experimental setup), averaging on their production position and energy. Care has been taken in order to ensure that a significant statistics was collected for all the relevant energies and emission positions allowing a measurement in which the dominant contribution to the uncertainty was systematic.

As the interactions with matter of the photons in the 1–20 MeV energy range is known to be very well reproduced in FLUKA, particular care has been made in setting up a simulation in which all the detector and experimental apparatus parts were properly included and positioned, especially those traversed by the photons in their path towards

the LYSO detector. The uncertainty related to the geometrical survey measurements and detector description details on the efficiency measurements are discussed in the systematic uncertainty section (§ 2.3).

## 2.2. Results

The production yields of prompt photons ( $\Phi_\gamma$ ) produced by  $^4\text{He}$ ,  $^{12}\text{C}$  and  $^{16}\text{O}$  ion beams, computed according to Eq. 1, measured with the detector in the angular configuration at  $90^\circ$  and  $60^\circ$ , with a deposited energy  $E > 2$  MeV, integrated over the full target size and averaged in a full  $4\pi$  solid angle, for the different ion beam energies are listed in Table 2. For each ion species,  $\Phi_\gamma$  increases with increasing energy, both at  $90^\circ$  and  $60^\circ$ , while no angular dependence is evidenced in the integrated production yield. Furthermore, as a first approximation, an universal behavior as a function of the primary energy exists independently of the nuclear species, as shown in Fig. 6.

It has to be noted that the results presented in this manuscript are related to the total integrated production of prompt photons occurring as a direct consequence of the interactions of primary ions with the target medium (primary component) that is limited up to the BP region and of the other indirect nuclear processes (secondary component) that can lead to a significant prompt photons production even after the BP region (Pinto et al. 2015). While the data collected with the most energetic  $^{12}\text{C}$  beam and the  $^4\text{He}$  and  $^{16}\text{O}$  beams had a BP position that was close (1 cm or less) to the exit (rear) PMMA face, and hence the secondary production of photons can be considered as similar and subdominant in all cases, particular care has to be taken when comparing the low energy carbon yields with results obtained in other experimental conditions. However, the nice agreement of the yields shown in Fig. 6 for the  $^{12}\text{C}$  beam at 120 MeV/u and the measurement presented in (Pinto et al. 2015) ( $^{12}\text{C}$  at 95 MeV/u) and in (Agodi et al. 2013) ( $^{12}\text{C}$  at 80 MeV/u) obtained in completely different experimental conditions are suggesting that the secondary component, while certainly present, is not dominant for those beam and (low) energy pair conditions.

The results from carbon ion beams have been compared with other results from literature. As reported in (Mattei et al. 2015), the prompt photon production yield obtained from a 220 MeV/u  $^{12}\text{C}$  beam impinging on a PMMA target, integrated over the full target size ( $5 \times 5 \times 20$  cm<sup>3</sup>) and averaged in a full  $4\pi$  solid angle, measured with a LYSO detector at the GSI (Darmstadt, Germany) facility is  $\Phi_\gamma(^{12}\text{C} \text{ 220 MeV/u}, E > 2 \text{ MeV @}90^\circ) = (6.3 \pm 0.2_{\text{stat}} \pm 2.1_{\text{sys}}) \times 10^{-3} \text{ sr}^{-1}$ . This experimental result is less than 3 standard deviation away from the correspondent HIT yield  $\Phi_\gamma$  shown in Table 2.

The production yield was also measured at GSI using a BaF<sub>2</sub> detector (Vanstalle et al. 2016) obtaining a value of  $\Phi_\gamma(^{12}\text{C} \text{ 220 MeV/u}, E > 2 \text{ MeV @}90^\circ) = (10.6 \pm 0.1_{\text{stat}} \pm 1.1_{\text{sys}}) \times 10^{-3} \text{ sr}^{-1}$ , in agreement within 1 standard deviation with the corresponding value shown in Table 2.

The measured yields were also compared with what presented in (Pinto et al. 2015), where the prompt- $\gamma$  absolute yield produced by a 95 MeV/u  $^{12}\text{C}$  beam interacting with

$\theta$	Ion	Energy (MeV/u)	$\Phi_\gamma \pm \sigma_{\text{stat}} \pm \sigma_{\text{sys}}$ ( $10^{-3} \text{ sr}^{-1}$ )
90°	$^4\text{He}$	125	$5.34 \pm 0.06 \pm 0.23$
		145	$6.53 \pm 0.07 \pm 0.27$
	$^{12}\text{C}$	120	$4.56 \pm 0.09 \pm 0.28$
		160	$7.59 \pm 0.13 \pm 0.35$
		180	$9.65 \pm 0.18 \pm 0.53$
		220	$12.19 \pm 0.24 \pm 1.11$
	$^{16}\text{O}$	210	$12.65 \pm 0.12 \pm 0.47$
		260	$16.83 \pm 0.20 \pm 0.65$
		300	$22.10 \pm 0.15 \pm 0.81$
60°	$^4\text{He}$	102	$3.70 \pm 0.08 \pm 0.11$
		125	$4.67 \pm 0.07 \pm 0.18$
		145	$6.40 \pm 0.08 \pm 0.27$
	$^{16}\text{O}$	210	$12.44 \pm 0.13 \pm 0.51$
		260	$17.04 \pm 0.19 \pm 0.69$
		300	$21.32 \pm 0.19 \pm 1.09$

**Table 2.** Production yields ( $\Phi_\gamma$ ) of prompt photons, computed according to Eq. 1, measured with the detector in the angular configuration at 90° and 60°, with a deposited energy threshold  $E > 2$  MeV, integrated over the full target size and averaged in a full  $4\pi$  solid angle, for the different ion beam energies. The statistical ( $\sigma_{\text{stat}}$ ) and systematic ( $\sigma_{\text{sys}}$ ) uncertainties are shown as well.

a PMMA target, with an energy threshold of 2 MeV, averaged over the full beam range, was reported to be  $(1.74 \pm 0.09_{\text{stat}} \pm 0.50_{\text{sys}}) \times 10^{-4} \text{ mm}^{-1} \text{ sr}^{-1}$ . In order to relate the integrated yield produced by the 120 MeV/u carbon ion beam shown in Table 2 with the Pinto’s result, we used an estimate of the full projected range for our beam of 30.86 mm, as estimated by SRIM 2013. With this assumption, the normalized rate becomes  $\Phi_\gamma(^{12}\text{C} \text{ 120 MeV/u @90°}) = (1.48 \pm 0.03_{\text{stat}} \pm 0.09_{\text{sys}}) \times 10^{-4} \text{ mm}^{-1} \text{ sr}^{-1}$ , in agreement with what measured in (Pinto et al. 2015).

### 2.3. Systematic uncertainties

Several sources are contributing to the total systematic uncertainty ( $\sigma_{\text{sys}}$ ) on the integrated absolute yield.

The  $N_\gamma$  value was computed using an unbinned maximum likelihood fit of the reduced ToF distributions. In order to evaluate the systematics related to the signal and background fit models, a different approach to count the signal events has been used. The background contribution in the signal region ( $\text{ToF}/\sigma_{\text{ToF}} \in [-3, 3]$ ) has been

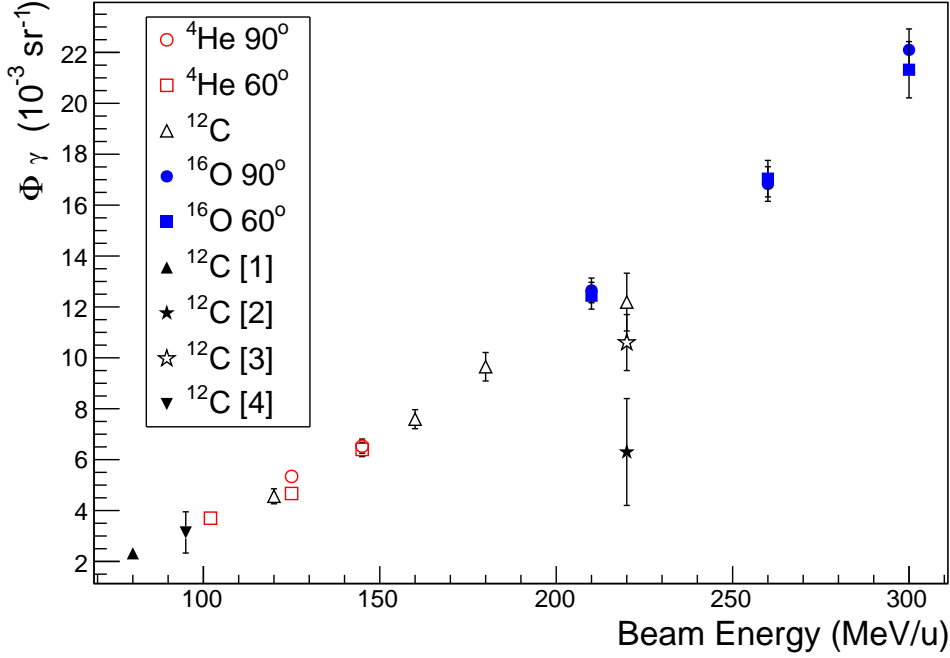


**Figure 6.** Production yields of prompt photons as a function of the primary beam energy for helium (open circle - 90°, open square - 60°), carbon (open up triangle) and oxygen (full circle - 90°, full square - 60°). The results from references [1] (Agodi et al. 2013), [2] (Mattei et al. 2015), [3] (Vanstalle et al. 2016) and [4] (Pinto et al. 2015) are superimposed.

extrapolated from the unbinned fit of the SideBands (SB) of the  $\text{ToF}/\sigma_{\text{ToF}}$  spectra ( $\text{ToF}/\sigma_{\text{ToF}} \in [-10, -3) \cup (3, 10]$ ). Therefore, the signal events have been computed as the total number of events in the signal region after the subtraction of the background as obtained from the SB extrapolation. The difference between the values obtained for  $N_\gamma$  from the SB subtraction method and the full fit analysis, significant only for the cases of  $^{12}\text{C}$  beams, has been used as an estimate of the systematic source from the  $N_\gamma$  evaluation and added in quadrature to  $\sigma_{\text{sys}}$  in the computation of the  $^{12}\text{C}$   $\Phi_\gamma$ . The relative contribution of the  $N_\gamma$  systematics to the total uncertainty varies from  $\sim 2\%$  up to  $\sim 8\%$ .

The measured total number of primaries  $N_{\text{ion}}^{\text{raw}}$  impinging on the PMMA target has been computed using the number of SCAND signals ( $N_{\text{SCAND}}$ ). In order to evaluate the systematic uncertainty due the  $N_{\text{SCAND}}$  evaluation, an independent measurement of  $N_{\text{ion}}^{\text{raw}}$  is necessary. It has been provided by the trigger line of the PET photons measurement, since the PET trigger is not related to the SC detector, though it is related to the true number of ions interacting in the target. The correlation between the number of PET triggers ( $N_{\text{PET}}$ ) and the SCAND signals has therefore been studied and founded to be within the statistical uncertainty of  $N_{\text{PET}}$ . Since this is the intrinsic limit of the systematic error on  $N_{\text{ion}}^{\text{raw}}$ , the statistical fluctuation of  $N_{\text{PET}}$  has been assigned as

systematic uncertainty to the estimated number of primaries. The relative contribution to the total uncertainty from this source ranges between  $\sim 3 - 6\%$ .

As already discussed beforehand, the  $N_{\text{ion}}^{\text{raw}}$  measurement has been corrected taking into account the inefficiency in the selection of multiple ions impinging on the SC at times smaller than 100 ns using the correction factor  $\text{corr}_{\text{ion}}$ . The details on the MC simulation that has been setup to account for this inefficiency are given in § 1.1. The systematic uncertainty due to this MC correction has been evaluated by performing a dedicated study in which the beam rate and the spill shape of the MC model have been varied within the uncertainties. The beam rate was changed from the value obtained by the data/MC agreement tuning to the mean value measured on data while the beam shape, obtained from a fit to the data sample, has been varied to take into account the uncertainties on the fit parameters and fit range. The relative contribution to the total uncertainty from this source varies from  $\sim 1\%$  up to  $\sim 5\%$ .

The systematic uncertainty on the total efficiency has been computed by using the FLUKA MC simulation and varying the simulated setup geometry, in order to account for the uncertainty on the relative positions of the different detectors and of the PMMA target, and beam size. The overall contribution to the total systematic uncertainty was found to be negligible in all cases.

The systematic error due to the maximum energy cut (10 MeV) in the  $N_\gamma$  integral computation has been checked against the MC simulation: the fraction of photons above that threshold ( $f_{\text{lost}}$ ) is of the order of 2‰ for the Helium and Carbon cases and for the Oxygen beam of 210 MeV at  $90^\circ$ . For the other Oxygen configurations  $f_{\text{lost}}$  is  $\sim 1\%$  and has been added to  $\sigma_{\text{sys}}$ .

Another possible systematic source to the yield evaluation is the 2 MeV lower limit of the energy range for the  $N_\gamma$  integral computation, due to possible energy shifts depending on the LYSO calibration curve. A systematic on the LYSO calibration has therefore been computed varying the calibration parameters of  $3\sigma$  around their mean values and taking into account their correlation coefficient: it is found to be negligible.

The systematic contribution coming from the background rejection of low energy charged particles using the  $N_{\text{hit}} < 3$  selection has been studied. Exploiting the MC simulation that reproduces the DCH number of hit data distribution, the raw  $N_\gamma$  integral has been computed asking for  $N_{\text{hit}} < 2$  and  $N_{\text{hit}} < 4$  and no significant variation has been observed.

### 3. Prompt- $\gamma$ monitoring applications

The research and development of particle therapy online monitoring devices relies on the experimental knowledge of the abundance and energy spectrum of secondary radiation produced by the incoming beam interaction with the patient body. As stated in the previous sections, the prompt photon radiation can be used to monitor the beam range inside the target during a PT treatment. The resolution achievable on the measured beam range depends on the production yield of prompt- $\gamma$ 's, their emission energy and

the technology that is used to detect them.

In order to have an estimate of the resolution achievable on the beam range using the prompt photons produced by the interaction of  $^4\text{He}$ ,  $^{12}\text{C}$  and  $^{16}\text{O}$  ion beams with a PMMA target, we used the results published in (Smeets et al. 2012), where the performances of a slit camera recently developed by the IBA are documented.

The results presented in (Smeets et al. 2012) have been obtained studying the prompt- $\gamma$ 's produced by the interactions of a 160 MeV proton beam impinging on a PMMA target. Figure 32 in (Smeets et al. 2012) shows the range estimation standard deviation as a function of the number of irradiated primary protons as measured by the IBA slit camera.

The use of a result obtained studying the interactions of a proton beam to assess the monitoring performances reachable in PT treatments with  $^4\text{He}$ ,  $^{12}\text{C}$  and  $^{16}\text{O}$  ion beams is possible, once the number of primary ions that have to be shot in order to deliver a given dose to a selected target volume (depth and dimensions fixed) is known.

Using a dedicated MC simulation it is possible to compute the number of primary ions in all the different configurations of ions ( $^4\text{He}$ ,  $^{12}\text{C}$  and  $^{16}\text{O}$ ) and energies of interest. The produced prompt photons in a given slice can hence be computed using the results presented in this manuscript and the detector performances (that are independent of the secondary radiation production source) properly assessed.

Two important implications of the proposed strategy have to be clarified:

- the number of primary ions that has to be shot in a real treatment to any target volume has a strong dependence on the details of the total tumor region under treatment. Beside the obvious dependence on the energy of the beam, for each slice under treatment the number of ions that have to be shot depends on the slice position within the total target volume, in order to account for the dose pile up and, also, of the RBE weight applied to each voxel. The assumptions that have been used to obtain the results presented in this manuscript are outlined below.
- the number of prompt photons that are emitted during the treatment has a dependence also on the material that is present after the BP: a secondary emission can occur, not directly related to the nuclear interactions of the primary beam particles with the target volume. The results obtained in this manuscript are related to the total prompt photons production, not having any experimental mean to disentangle the two different production mechanisms. Hence, the flux used to compute the final number of photons has a direct dependence on the experimental conditions used to obtain the results presented in table 2, as discussed in § 2.2.

The study documented in this manuscript refers to two distinct and well defined treatment configurations, studied using a dedicated FLUKA MC simulation. The first one to be used as a reference (a) while the second one represents a real case scenario as described by (Krämer et al. 2000) (b):



- a) 1 Gy dose homogeneously distributed in a slice of 3 mm centered on the Bragg peak position at a depth in PMMA of  $\sim 85$  mm;
- b) 1 Gy dose delivered to a tumor of  $120 \text{ cm}^3$ , divided in 39 slices.

The conclusions, that are related to the number of prompt photons generated in the well defined scenarios are an indication of the expected number of produced photons in conditions that are, under some assumptions, not far from typical treatment conditions but are not meant to be used as representative of the final performances attainable on generic PT treatments, as those will have to be assessed using dedicated full MC simulations.

In both cases, the number of primary  $^4\text{He}$ ,  $^{12}\text{C}$  and  $^{16}\text{O}$  ions of a given energy needed to deliver the desired dose has been evaluated and is, in the  $^{12}\text{C}$  case, of the same order of magnitude of the number of ions used in real treatments performed at CNAO. The physical dose (1 Gy) has been chosen as a reference considering that the RBE weighted dose is of the order of  $\sim 2$  RBE-Gy and that in a PT treatment at CNAO, using two laterally-opposed carbon-ion beams, a value of an RBE-weighted dose of 70.4 RBE-Gy divided in 16 fractions of 4.4 RBE-Gy each was prescribed to a skull-base chordoma target volume ( $\sim 2$  RBE-Gy for each beam) (Russo et al. 2016). We thus used the 1 Gy value as representative of the total RBE weighted dose, averaged against the SOBP region, for a given PT with heavy ions. Such assumption, and the related conclusions, can be translated to different total doses to account for different details of the treatment under study using a dedicated MC simulation. However the conclusions on the feasibility of prompt photons monitoring do not change, as they are related to the order of magnitude of the emitted photons.

The expected prompt photons absolute yields have been estimated using the results reported in Table 2, in the  $90^\circ$  angular configuration.

For the *a* configuration, the number of primaries predicted by the MC simulation and the relative amount of prompt- $\gamma$ 's produced are reported in Table 3. As previously outlined, (Smeets et al. 2012) quoted the standard deviation on the estimated beam range using the prompt photon radiation as a function of the number of 160 MeV primary protons irradiating a PMMA target. Hence, using the measurement of the prompt photon yield emitted by a 160 MeV proton beam reported in (Pinto et al. 2015), we computed the number of primary protons needed to produce the prompt- $\gamma$  absolute yields listed in the last column of Table 3. For  $^4\text{He}$  beam we obtained  $\sim 4 \times 10^8$  primary protons, for  $^{12}\text{C}$  and  $^{16}\text{O}$  beams we obtained  $\sim 2 \times 10^8$  protons and, hence, an expected standard deviation on the beam range estimation that is less than 2 mm.

These preliminary results can be used as a basis to discuss the prompt photons applications to beam range monitoring in the scenario of a real treatment plan, described in the *b* configuration. In (Krämer et al. 2000) a total number of  $\sim 7 \times 10^8$  carbon ions is needed to deliver 1 Gy of absorbed dose to a tumor of  $120 \text{ cm}^3$  divided in 39 slices. As an exercise, assuming that each energy slice is irradiated with  $\sim 2 \times 10^7$

Beam	Number of Primaries	Absolute Yield ( $\times 10^5$ counts/sr)
$^4\text{He}$ 125 MeV/u	$1.9 \times 10^8$	$(10.15 \pm 0.11_{\text{stat}} \pm 0.44_{\text{sys}})$
$^{12}\text{C}$ 220 MeV/u	$4.4 \times 10^7$	$(5.36 \pm 0.11_{\text{stat}} \pm 0.49_{\text{sys}})$
$^{16}\text{O}$ 260 MeV/u	$2.4 \times 10^7$	$(4.04 \pm 0.05_{\text{stat}} \pm 0.16_{\text{sys}})$

**Table 3.** Number of primary particles needed to deliver a physical dose of 1 Gy in a slice of 3 mm centered on the BP position ( $\sim 85$  mm depth) in a PMMA target as predicted from a FLUKA MC simulation. The corresponding prompt photons absolute yield is reported in the last column, computed using the measurements shown in Table 2.

$^{12}\text{C}$  ions of 220 MeV/u, we computed the expected absolute prompt photon yield per slice that is  $(2.44 \pm 0.05_{\text{stat}} \pm 0.22_{\text{sys}}) \times 10^5$  counts/sr. If 125 MeV/u  $^4\text{He}$  and 260 MeV/u  $^{16}\text{O}$  ion beams are considered, to deliver the same physical dose of  $2 \times 10^7$   $^{12}\text{C}$  ions a number of  $\sim 8.6 \times 10^7$   $^4\text{He}$  and  $\sim 1.1 \times 10^7$   $^{16}\text{O}$  is needed, producing a  $\gamma$  yield of  $(4.59 \pm 0.05_{\text{stat}} \pm 0.20_{\text{sys}}) \times 10^5$  and  $(1.85 \pm 0.02_{\text{stat}} \pm 0.07_{\text{sys}}) \times 10^5$  counts/sr respectively. The expected resolutions when using a slit camera have been computed for the real case scenario as done before for the *a* configuration: the number of equivalent 160 MeV primary protons needed to produce the predicted prompt- $\gamma$  yields from  $^4\text{He}$ ,  $^{12}\text{C}$  and  $^{16}\text{O}$  ions has been estimated. The obtained relative expected standard deviation on the beam range estimation has values smaller than 3 mm for  $^{12}\text{C}$  and  $^{16}\text{O}$  and smaller than 2 mm for  $^4\text{He}$ .

It has to be noticed that physical doses larger than 1 Gy can be delivered in a typical treatment fraction, and hence our estimate of the achievable resolution on the beam range can be considered as conservative. Furthermore, we would like to point out that in hypofractionated treatments the relevance of a possible real-time monitoring will be particularly significant. Our results support the conclusion that monitoring techniques exploiting prompt photons are feasible in particle therapy, providing a resolution on the beam range matching the clinical requirements.

To evaluate the monitoring performances in real treatment cases, it is necessary to take into account all the patient/treatment specific characteristics, like the tumor volume, its location inside the body and the different tissues that have to be traversed by the beam. A systematic study of the impact on the prompt gamma monitoring performances of the target inhomogeneities will be performed in the future, testing different geometrical configurations and beam energies. Furthermore, a substantial contribution to predictions when considering a real treatment scenario can also be provided from the Monte Carlo simulations, progressively updated with experimental data measurements.

## Conclusions

The prompt photon production of  $^4\text{He}$ ,  $^{12}\text{C}$  and  $^{16}\text{O}$  beams interacting with a beam stopping PMMA target has been studied at the HIT Heidelberg facility with beam energies of interest for PT applications. The production yield measurements performed in this study using  $^{12}\text{C}$  ions beam are found to be in agreement with results obtained from other experiments.

The  $^4\text{He}$  and  $^{16}\text{O}$  beams, whose prompt- $\gamma$  production is herein measured for the first time, are particularly relevant for future PT applications. The obtained results confirm that a non negligible prompt photons production occurs in the interactions of  $^4\text{He}$  and  $^{16}\text{O}$  beams of therapeutical energy with a PMMA target.

The measured yields have been used to compute the expected resolution on the beam range in a typical treatment scenario, assuming the performances of the IBA slit camera documented in (Smeets et al. 2012). Resolutions below 2 – 3 mm are obtained in all the different scenarios supporting the feasibility of a prompt photons based beam range monitoring approach for PT using  $^4\text{He}$ ,  $^{12}\text{C}$  or  $^{16}\text{O}$  particle beams.

## Acknowledgements

We would like to thank sincerely Marco Magi (SBAI Department) for his valuable effort in the construction of several mechanical supports of the experimental setup. This work has been partly supported by the “Museo storico della Fisica e Centro di studi e ricerche Enrico Fermi”. The access to the test beam at the Heidelberg Ion-beam Therapy center has been granted by the ULICE European program. We are indebted to Prof. Dr. Thomas Haberer and Dr. Stephan Brons for having encouraged this measurement, made possible thanks to their support and to the help of the whole HIT staff.

## References

- Abou-Haidar Z et al. 2012 Performance of upstream interaction region detectors for the first experiment at gsi *Journal of Instrumentation* **7**, P02006.
- Agodi C et al. 2012a Charged particle’s flux measurement from pmma irradiated by 80 mev/u carbon ion beam *Physics in Medicine and Biology* **57**, 5667.
- Agodi C et al. 2012b Precise measurement of prompt photon emission from 80 mev/u carbon ion beam irradiation *Journal of Instrumentation* **7**, 03001.
- Agodi C et al. 2012c Study of the time and space distribution of beta+ emitters from 80 mev/u carbon ion beam irradiation on pmma *Nuclear Instruments and Methods in Physics Research Section B* **283**, 5667.
- Agodi C et al. 2013 Erratum: Precise measurement of prompt photon emission from 80 mev/u carbon ion beam irradiation *Journal of Instrumentation* **8**(11), E11002.
- Attanasi F et al. 2009 Comparison of two dedicated in beam pet systems via simultaneous imaging of  $^{12}\text{C}$ -induced  $\beta^+$ -activity *Physics in Medicine and Biology* **54**, 29.
- Battistoni G et al. 2015 Overview of the fluka code *Annals of Nuclear Energy* **82**, 10–18.

- Bellini F et al. 2014 Extended calibration range for prompt photon emission in ion beam irradiation *Nuclear Instruments and Methods in Physics Research Section A* **745C**, 14.
- Boehlen T T et al. 2014 The fluka code: Developments and challenges for high energy and medical applications *Nuclear Data Sheets* **120**, 211–214.
- Enghardt W et al. 2004 Charged hadron tumour therapy monitoring by means of pet *Nuclear Instruments and Methods in Physics Research Section A* **25**, 284.
- Ferrari A et al. 2005 Fluka: a multi particle transport code *Tech. Rep. CERN-2005-10 INFN/TC05/11*.
- Fiedler F et al. 2008 In-beam pet measurements of biological half-lives of  $^{12}\text{C}$  irradiation induced  $\beta^+$ -activity *Acta Oncologica* **47**, 1077.
- Fuchs H et al. 2014 Oc-0393: Can particle beam therapy be improved using helium ions? - a treatment planning study focusing on pediatric patients *Radiotherapy and Oncology* **111**, S154.
- Gwosch K et al. 2013 Non-invasive monitoring of therapeutic carbon ion beams in a homogeneous phantom by tracking of secondary ions *Physics in Medicine and Biology* **58**, 3755.
- Henriquet P et al. 2012 Interaction vertex imaging (ivi) for carbon ion therapy monitoring: a feasibility study *Physics in Medicine and Biology* **54**, 4655.
- Kraan A 2015 Range verification methods in particle therapy: underlying physics and monte carlo modeling *Frontiers in Oncology* **Article 150**.
- Krämer M et al. 2000 Treatment planning for heavy-ion radiotherapy: physical beam model and dose optimization *Physics in Medicine and Biology* **45**, 3299–3317.
- Kurz C, Mairani A & Parodi K 2012 First experimental-based characterization of oxygen ion beam depth dose distributions at the heidelberg ion-beam therapy center *Physics in Medicine and Biology* **57**(15), 5017.  
**URL:** <http://stacks.iop.org/0031-9155/57/i=15/a=5017>
- Loeffler J S & Durante M 2013 Charged particle therapy – optimization, challenges and future directions *Nature Reviews Clinical Oncology* **10**, 411– 424.
- Marafini M & et al. 2015 The inside project: innovative solutions for in-beam dosimetry in hadrontherapy *Acta Physica Polonica A* **127**, 1465.
- Mattei I et al. 2015 Prompt- $\gamma$  production of 220 mev/u  $^{12}\text{C}$  ions interacting with a pmma target *Journal of Instrumentation* **10**(10), P10034.
- Parodi K et al. 2002 In-beam pet measurements of  $\beta^+$  radioactivity induced by proton beams *Physics in Medicine and Biology* **47**, 21.
- Parodi K et al. 2008 Comparison between in-beam and offline positron emission tomography imaging of proton and carbon ion therapeutic irradiation at synchrotron- and cyclotron-based facilities *International Journal of Radiation Oncology · Biology · Physics* **71**, 945–956.  
**URL:** <http://dx.doi.org/10.1016/j.ijrobp.2008.02.033>
- Parodi K et al. 2012 Monte carlo simulations to support start-up and treatment planning of scanned proton and carbon ion therapy at a synchrotron-based facility *Physics in Medicine and Biology* **57**(12), 3759.
- Pawelke J et al. 1997 In-beam pet imaging for the control of heavy-ion tumour therapy *IEEE Trans. Nucl. Sci.* **44**, 1492.
- Pennazio F & et al. 2015 A study of monitoring performances with the inside system *Acta Physica Polonica A* **127**, 1468.
- Piersanti L et al. 2014 Measurement of charged particle yields from pmma irradiated by a 220 mev/u  $^{12}\text{C}$  beam *Physics in Medicine and Biology* **59**, 1857.
- Pinto M et al. 2015 Absolute prompt-gamma yield measurements for ion beam therapy monitoring *Physics in Medicine and Biology* **60**, 565–594.
- Priegnitz M & et al. 2008 In-beam pet measurement of  $^7\text{Li}^{3+}$  irradiation induced beta+-activity. *Phys. Med. Biol.* **53**(16), 443.
- Russo G et al. 2016 A novel algorithm for the calculation of physical and biological irradiation quantities in scanned ion beam therapy: the beamlet superposition approach *Physics in Medicine and*

- Biology* **61**, 183–214.
- Skwarnicki T 1986 A study of the radiative CASCADE transitions between the Upsilon-Prime and Upsilon resonances PhD thesis.
- Smeets J et al. 2012 Prompt gamma imaging with a slit camera for real-time range control in proton therapy *Physics in Medicine and Biology* **57**, 3371.
- Testa E et al. 2008 Monitoring the bragg peak location of 73 mev/u carbon ions by means of prompt  $\gamma$ -ray measurements *Applied Physics Letters* **93**, 093506.
- Testa E et al. 2009 Dose profile monitoring with carbon ions by means of prompt-gamma measurements *Nuclear Instruments and Methods in Physics Research Section B* **267**, 993.
- Testa M et al. 2010 Real-time monitoring of the bragg-peak position in ion therapy by means of single photon detection *Radiation and Environmental Biophysics* **49**, 337–343.
- Tommasino F, Scifoni E & Durante M 2015 New ions for therapy *International Journal of Particle Therapy* **2**(3), 428–438.
- Vanstalle M et al. 2016 Measurement of prompt- $\gamma$  yields and spectra for hadrontherapy monitoring *Submitted for publication in Physics in Medicine and Biology* .
- Vecchio S et al. 2009 A pet prototype for in-beam monitoring of proton therapy *IEEE Trans. Nucl. Sci.* **56**, 1.
- Verkerke W & Kirkby D 2003 The roofit toolkit for data modeling *arXiv:physics/0306116* .